

This is the accepted version of the following article

Roman Svoboda (2019). Crystallization of $(\text{GeSe}_2)_{0.3}(\text{Sb}_2\text{Se}_3)_{0.7}$ chalcogenide glass - Influence of reaction atmosphere. *Journal of Non-Crystalline Solids*. DOI: 10.1016/j.jnoncrysol.2018.12.034

This accepted version is available from URI <https://hdl.handle.net/10195/74728>

Publisher's version is available from:

<https://www.sciencedirect.com/science/article/pii/S0022309319300626?via%3Dihub>



This version is licenced under a [Creative Commons Attribution-NonCommercial-NoDerivatives 4.0 International](https://creativecommons.org/licenses/by-nc-nd/4.0/).

Crystallization of $(\text{GeSe}_2)_{0.3}(\text{Sb}_2\text{Se}_3)_{0.7}$ chalcogenide glass - influence of reaction atmosphere

Roman Svoboda*

Department of Physical Chemistry, Faculty of Chemical Technology, University of Pardubice, Studentská 573, 532 10 Pardubice, Czech Republic.

Abstract

Differential scanning calorimetry, infrared microscopy and X-ray diffraction analysis and were used to investigate the influence of reaction atmosphere (air versus pure nitrogen) on crystallization behavior of $(\text{GeSe}_2)_{0.3}(\text{Sb}_2\text{Se}_3)_{0.7}$ glass. The presence of oxygen was found to accelerate the crystal growth both on surface and in bulk material, with a similar effect in case of powders and bulk samples. Detailed crystallization kinetics study was performed, revealing that the presence of oxygen leads to a lowered activation energy and steeper onset of the process – single-curve-averaged masterplot approach was used to deal with the temperature-differentiated complexity of the crystallization. Direct observations by infrared microscopy have shown that the presence of oxygen leads to a formation of robust surface crystalline layer, which prevents powder sintering and bulk samples deformation by viscous flow, and to a more rapid nucleation and crystal growth within the sample volume. Based on the viscosity values estimated for the crystallization temperatures, an explanation for the accelerated volume crystallization was proposed, employing the quasi-stationary conditions contributing to better cohesivity of critical nuclei and crystal/glass interface. The existence of the surface crystalline layer however prevents the sample from reaching full crystallinity.

Keywords: crystallization kinetics, reaction atmosphere, DSC, XRD, infrared microscopy, $(\text{GeS}_2)_{0.3}(\text{Sb}_2\text{S}_3)_{0.7}$ glass

* Corresponding author: Tel.: +420 466 037 346 E-mail address: roman.svoboda@upce.cz

1. Introduction

Crystallization behaviour is one of the most often studied thermal properties for chalcogenide glasses (over 1300 articles found on Web of Science; “crystallization AND chalcogenide glass”, 2018). Large majority of these studies were performed by using either differential scanning calorimetry (DSC) or differential thermal analysis (DTA) techniques. Whereas the influences of e.g. long-term degradation [1-3], particle size [4-8] or investigated temperature range (during non-isothermal measurements determined by the heating rate) [9-11] on the DSC/DTA crystallization measurements of chalcogenide glasses are relatively well documented, the influence of the reaction atmosphere has been neglected for the past decades. It has been shown only recently [12 - 14] that for the $(\text{GeS}_2)_x(\text{Sb}_2\text{S}_3)_{1-x}$ glasses the conventional way utilized during the DSC measurements (hermetic sealing of the sample into the DSC pan, i.e. sample being surrounded by air atmosphere) provides significantly different results compared to the sample being measured in an open pan in the flow of the nitrogen atmosphere (this way of measurement is generally avoided in case of chalcogenides due to their tendency toward sublimation and the consequent ability to irreversibly contaminate the DSC cell and/or destroy the Pt-based thermocouples). It has been shown in [12] that the presence of oxygen accelerates crystallization from mechanically induced defects for Sb_2S_3 -rich compositions and sustains the intensity of crystal formation in case of the Sb_2S_3 -poorer materials. Furthermore, based on the viscosities and microscopically determined crystal growth rates it was concluded that it is the markedly higher crystal growth rate that is responsible for the $(\text{GeS}_2)_{0.1}(\text{Sb}_2\text{S}_3)_{0.9}$ composition being more prone to the influence of oxygen on the crystal growth.

Since the $(\text{GeS}_2)_x(\text{Sb}_2\text{S}_3)_{1-x}$ glasses investigated in [12 - 14] crystallize strictly from surface, in the present study we have decided to investigate in a similar way the selenium counterpart of these materials (namely the $(\text{GeSe}_2)_{0.3}(\text{Sb}_2\text{Se}_3)_{0.7}$ composition), which is known

to crystallize also in bulk volume. Detailed study of the crystallization and of its kinetics will be performed in order to reveal the possible differences in oxygen influence on the crystal growth in chalcogenide glasses. The study will be performed in dependence on particle size in order to investigate how the crystal growth is affected by the presence of oxygen. Note that the above-mentioned composition is effectively the counterpart for the $(\text{GeS}_2)_{0.1}(\text{Sb}_2\text{S}_3)_{0.9}$ glass, as both are the Sb-richest materials that can be prepared by conventional melt-quench method. Similarly as the Ge-Sb-S materials, also the Ge-Sb-Se glasses are utilized mainly in near-infrared optics applications. [15 - 20]

2. Experimental

The $(\text{GeSe}_2)_{0.3}(\text{Sb}_2\text{Se}_3)_{0.7}$ glass was prepared by the standard melt-quench method. Pure elements (5N, Sigma Aldrich) were inserted in a fused silica ampoule, which was evacuated annealed in a rocking furnace at 950 °C for 24 h and then quenched in water. The ingot of chalcogenide glass was crushed in agate mortar, ground and sieved (via the sieves with defined mesh sizes) in order to prepare the following powder particle size fractions: 20 – 50, 125 – 180 and 300 - 500 μm . Thin sheets of glass formed on the inner sides of the ampoule were used as bulk samples (minimum amount of mechanically induced defects [21] was achieved in this way). All the above-mentioned operations including the consequent storing were performed on air.

Crystallization of the $(\text{GeSe}_2)_{0.3}(\text{Sb}_2\text{Se}_3)_{0.7}$ glass was studied by Q2000 heat-flow DSC (TA Instruments) equipped with an autosampler, RCS90 cooling accessory, and T-zero technology. The instrument was calibrated using In, Zn, and H_2O ; dry N_2 was used as purge gas at a flow rate of 50 $\text{cm}^3 \cdot \text{min}^{-1}$. Fresh zero-line calibration was performed before the measurements. Two sets of non-isothermal experiments were performed for each $(\text{GeSe}_2)_{0.3}(\text{Sb}_2\text{Se}_3)_{0.7}$ particle size: during the first set of measurements the samples were

heated in open pans so that the DSC purge gas (N₂) acted as protective atmosphere, during the second set of measurements the pans with samples were hermetically sealed so that the air enclosed in the pan could oxidize the chalcogenide glass. Each set of measurements consisted of the following heating rates - 0.5, 1, 2, 5, 10 and 20 °C·min⁻¹. Selected measurements were reproduced to confirm good repeatability and validity of the results.

X-ray diffraction technique (XRD) and Raman spectroscopy were used to confirm the amorphous character of the prepared material (it was also verified that the pre-measurement glass processing did not cause crystallization) and identify the crystalline products obtained during the DSC measurement. The XRD analysis of amorphous and crystalline samples was performed using a Bruker AXS diffractometer D8 Advance equipped with a horizontal goniometer and scintillation counter utilizing CuK_α radiation. The Raman measurements were performed by DXR2 Raman microscope (Thermo Fisher Scientific) utilizing 780 nm excitation laser (1 mW, 60 scans → 5 s each; laser spot size equal to 3.1 μm) and CCD detector. The crystalline products were examined also by means of the infrared microscope Olympus BX51 equipped with XM10 camera (reflection mode).

3. Results

The crystallization data obtained by DSC for each particle size and both atmospheres are depicted in Figs. 1 and 2. Each pair of corresponding graphs with data obtained under the two respective atmospheres has similar scaling on both the temperature and heat flow axes for easier comparison. All crystallization signals are already corrected for the influence of the system heat capacity (and its temperature evolution) – the tangential area-proportional baseline [22] was used. The crystallization proceeding in air appears to be slightly shifted to lower temperatures (which may suggest an accelerating influence of the oxidizing atmosphere); this effect increases in magnitude with increasing particle size d_{aver} . Moreover,

the crystal growth in air exhibits a higher-order kinetics – with increasing heating rate q^+ the onsets of the DSC peaks are well separated. Interestingly, the differences in crystallization behaviour persist throughout the whole spectrum of tested particle sizes, which indicates that the changes induced by the oxygen presence (supposedly on the surface of the glass grains) propagate through the bulk of the material – this phenomenon will be further discussed in Section 4. In addition, it is interesting to note that with increasing particle size the DSC peaks shift to higher temperatures only very marginally – this is usually a sign of crystal growth proceeding mainly in the material volume (as opposed to the material surface), as will be indeed in section 4.2. confirmed via infrared microscopy. This effect is again present for both the air and N_2 atmospheres, as would be expected for the $(GeSe_2)_x(Sb_2Se_3)_{1-x}$ glass crystallizing dominantly in volume.

Structural characterization of the as-prepared glass and the DSC-crystallized materials is shown in Fig. 3. The Raman measurements performed for randomly selected samples of the as-prepared glass (measured on both, surface and break fracture) confirmed homogeneity of the glass – see the upper two spectra in Fig. 3A. The Raman measurements of DSC-crystallized samples have also confirmed similarity of the formed crystalline products – see the lower two spectra in Fig. 3B. The Raman peaks within the main band can be assigned as follows: 155 cm^{-1} Sb-Sb vibration in $Se_2Sb-SbSe_2$ units [23-25], 170 cm^{-1} (plus the weak signal at 270 cm^{-1}) Ge-Ge vibration in $Ge_2Se_{6/2}$ and $Ge-Ge_ySe_{4-y}$ ($y = 1-4$) units [24, 26-28], 190 cm^{-1} Sb-Se stretch vibration in $SbSe_{3/2}$ pyramids [24, 25, 29], 200 cm^{-1} asymmetric stretch vibration in corner-shared $GeSe_{4/2}$ tetrahedra [23, 24, 29], 215 cm^{-1} A1 breath vibration in edge-shared $GeSe_{4/2}$ tetrahedra [27-29], and 265 cm^{-1} A1 vibrations in Se_n chains, and dimers or short chains of corner-shared $GeSe_{4/2}$ tetrahedra [23, 24, 29]. Note however that Raman spectroscopy is primarily surface sensitive. Information about the overall similarity of the crystallization products formed under the two atmospheres was provided by XRD (see

Fig. 3B), which confirmed presence of the orthorhombic Sb_2Se_3 (Pbnm 62) crystalline phase. The diffraction patterns depicted in Fig. 3B as well as the cell parameters and average crystallite size calculated according the Scherrer formula indicate complete similarity of the two crystalline products: N_2 – $a = 11.62672$, $b = 11.77852$, $c = 3.97440$, crystallite size 317.8 Å; O_2 – $a = 11.62364$, $b = 11.77922$, $c = 3.97207$, crystallite size 329.3 Å.

4. Discussion

4.1. Analysis of the DSC data

The crystallization kinetics of the $(\text{GeSe}_2)_{0.3}(\text{Sb}_2\text{Se}_3)_{0.7}$ glass was described by means of the standard kinetic equation [30]:

$$\Phi = \Delta H \cdot A \cdot e^{-E/RT} \cdot f(\alpha) \quad (1)$$

where Φ is the measured heat flow, ΔH is the crystallization enthalpy, A is the pre-exponential factor, E is the apparent activation energy of the process, R is the universal gas constant, T is temperature and $f(\alpha)$ stands for an expression of a kinetic model with α being conversion. The enumeration of Eq. 1 can be done by a number of methods [31]. Nowadays, the most popular are the nonlinear optimization methods (e.g. multivariate kinetic analysis MKA [32], see Eqs. 2 and 3), which provide the possibility of simultaneous fit of all obtained DSC curves. In the present study the MKA was employed for the three most common kinetic models, the nucleation-growth Johnson-Mehl-Avrami model [33-36] (JMA, see Eq. 4), the empirical autocatalytic Šesták-Berggren model [30] (AC, see Eq. 5) and the empirical model of autocatalyzed n^{th} -order reaction (NC, see Eq. 6):

$$RSS = \sum_{j=1}^n \sum_{k=First_j}^{Last_j} w_{j,k} (Y \exp_{j,k} - Ycal_{j,k})^2 \quad (2)$$

$$w_{j,k} = \frac{\sum_{j=1}^n (Last_j - First_j)}{n(Last_j - First_j) [abs(Max(Y \exp_{j,k})) + abs(Min(Y \exp_{j,k}))]} \quad (3)$$

$$f(\alpha) = m(1-\alpha)[- \ln(1-\alpha)]^{-(1/m)} \quad (4)$$

$$f(\alpha) = \alpha^M (1-\alpha)^N \quad (5)$$

$$f(\alpha) = (1 + K\alpha)(1-\alpha)^n \quad (6)$$

where RSS is the sum of squared residue, n is number of measurements, j is index of the given measurement, $First_j$ is the index of the first point of the given curve, $Last_j$ is the index of the last point of the given curve, $Y_{exp,j,k}$ is the experimental value of the point k of curve j , $Y_{cal,j,k}$ is the calculated value of the point k of curve j and $w_{j,k}$ is weighting factor for the point k of curve j (the weighting factor was optimized for the DSC measurements, so that each measured curve is weighted despite the different number of measured points and increased errors due to the magnifying influence of heating rate), and m , M , N , n and K are the kinetic parameters of the respective models.

However, in case of the present data the simultaneous optimization of all measured curves within each set provided very poor description of the kinetic data. The statistic results (correlation coefficients r^2 and F-test values) are displayed in Table 1 for each model and kinetic dataset. As is apparent, the simultaneous fits resulted in unacceptably low correlation coefficients and inconsistent variability of the suitability of the tested kinetic models – the main problems were the DSC peaks obtained at lowest q^+ shifted to slightly lower temperatures than predicted based on the kinetics of the rest of the datasets, and the slightly inconsistent asymmetry of the kinetic peaks evolving with q^+ (this is a common, often neglected issue, recently pointed out e.g. in [10]). Therefore we have adopted an alternative approach based on the linearization methods, with the model-free evaluations employing the Kissinger [37] (Eq. 7) and Friedman [38] (Eq. 8) equations and the model-based calculations based on averaging (over the different applied q^+) the results from the master plots $z(\alpha)$ and $y(\alpha)$ [39] (Eqs. 9 and 10):

$$\ln\left(\frac{q^+}{T_p^2}\right) = -\frac{E}{RT_p} + const. \quad (7)$$

$$\ln(\Phi_\alpha) = -\frac{E}{RT_\alpha} + \text{const.} \quad (8)$$

$$y(\alpha) = \Phi \cdot e^{E/RT} \quad (9)$$

$$z(\alpha) = \Phi \cdot T^2 \quad (10)$$

where T_p is the temperature corresponding to the maximum of the crystallization peak, Φ_α and T_α are the specific heat flow and temperature corresponding to certain chosen value of conversion α .

Starting with the crystallization enthalpy (see Fig. 4A), the presence of oxygen appears to decrease the overall amount of crystalline products formed during the heating in DSC – approx. $45 \text{ J}\cdot\text{g}^{-1}$ versus ca. $60 \text{ J}\cdot\text{g}^{-1}$ in case of crystallization under nitrogen. Similar decrease of ΔH is observed also for the finest powder being crystallized under nitrogen, which indicates that the decrease may be associated either with large amounts of mechanically induced defects hindering the volume crystallization (the case of the N_2 atmosphere) or with the surface being activated/oxidized (again restricting the growth – the exact mechanism will be discussed later in this section). The activation energies determined by the Kissinger and Friedman (the E - α dependences were averaged in the $0.3 - 0.7 \alpha$ region) methods are shown in Fig. 4B. The significantly higher activation energies found for the N_2 -crystallized samples corresponds with the kinetic behavior depicted in Figs. 1 and 2 as well as with the O_2 -based crystallization being slightly faster. The rise of E with decreasing d_{aver} is quite common for chalcogenides and can be explained by the restrictions to the crystal growth caused by both surface- and volume-located defects originating from the grinding procedure. The model-based linearization (described e.g. in [40]) was used to calculate the kinetic exponents of the most commonly used kinetic model – the AC equation (Eq. 5), see Fig. 4C. The AC model parameters suggest that a significantly different model-based kinetics drives the dominant crystallization processes in cases of air and nitrogen atmospheres; in addition the O_2 -based crystallization exhibits a slight development with d_{aver} . In order to specify the crystal growth

micro-mechanism, the description in terms of the physically meaningful JMA model was also employed – the maxima of the $z(\alpha)$ masterplot (see Fig. 4D) very well correspond to the JMA fingerprint value of 0.632, indicating that the present data can indeed be described by this model. The maxima of the $y(\alpha)$ function then correspond to the JMA kinetic exponents 1.4 and 3.1 for the N_2 -based and O_2 -based crystallizations, respectively, corresponding to the effective 1-D and 3-D respective crystallite morphologies.

4.2. Analysis of the microscopic data

Since the presence of oxygen was found to alternate large number of aspects of the $(GeSe_2)_{0.3}(Sb_2Se_3)_{0.7}$ glass crystallization behavior, infrared microscopy was used to directly investigate the initial stages of the crystallization process. For this reason several bulk samples were heated in DSC at $5\text{ }^\circ\text{C}\cdot\text{min}^{-1}$ to the selected temperatures (288 and 294 $^\circ\text{C}$) either under the N_2 or air atmosphere, and then rapidly cooled down to preserve the achieved state of crystallinity. The representative micrographs are depicted in Figs. 5 and 6 for the N_2 -crystallized and O_2 -crystallized samples, respectively. Left columns depict the surfaces, right columns depict the cross-section views; upper rows show the micrographs obtained at 288 $^\circ\text{C}$, low rows of micrographs show the materials heated to 294 $^\circ\text{C}$. It is apparent that the O_2 -crystallized samples exhibit rather robust surface layers of crystalline material (as opposed to the almost complete lack of surface crystallinity in case of the N_2 -crystallized samples), which can certainly be attributed to the oxygen activating the surface crystal growth centers. The most distinctive difference between the two sets of micrographs is however the markedly larger amount and larger size of the developed crystallites in case of the O_2 -crystallized samples – it needs to be stressed that this applies not only for the surface but also for the crystals found in the inner volume (see the cross-section micrographs). This feature very well corresponds to the generally faster crystallization (occurring at lower temperatures) that was

demonstrated in Figs. 1 and 2; note that the formation of the surface crystalline layer in case the O₂-crystallized samples (which is essentially independent from d_{aver}) is also responsible for the similar onset temperatures of the O₂-crystallization DSC peaks obtained at low q^+ (where the development of the continual surface layer is not kinetically hindered).

Nevertheless, since the diffusion of O₂ into the chalcogenide material is orders of magnitude slower than the timeframe given by the DSC experiment, the sole existence of the chalcogenide/air interface does not explain the marked increase in volume nucleation and crystal growth rapidity (both velocities are likely to be affected since the comparison of micrographs clearly shows larger number of crystallites, which are in addition also significantly bigger). The only possible explanation appears to be therefore associated with the existence of the robust surface crystalline layer. Such layer does to a certain extent influence [41] the internal pressure within the glass as well as the conditions for diffusion (note the incongruent crystallization of Sb₂Se₃, requiring movement of antimony towards the growth interface and recession of germanium away from the interface). Similar effect was earlier studied in detail for the As₂Se₃ chalcogenide glass – it was shown that presence of even a relatively small amount of crystallites can influence the viscosity of the material to such an extent that crystal growth ceases. [41] Based on the compositional extrapolation of the viscosity data published in [42], viscosity of the (GeSe₂)_{0.3}(Sb₂Se₃)_{0.7} glass at 290 °C is approx. $\log(\eta/\text{Pa}\cdot\text{s}) = 5.5$, which is well below the Littleton softening point ($\log(\eta/\text{Pa}\cdot\text{s}) = 6.6$; glass deforms under its own weight), approaching the flow point ($\log(\eta/\text{Pa}\cdot\text{s}) = 4$) - the low viscosity was qualitatively confirmed also by simple examination of the DSC-crystallized bulk samples, where the N₂-crystallized were markedly deformed with largely round edges and the powdered material sintered, whereas the O₂-crystallized samples preserved their original shape. Considering the mechanistic influence of the robust surface crystalline layer retaining the shape of the crystallizing grain of glass, at such low viscosity the inner glass

pressure will be negligible and the potentially lower viscosity itself (which is at given temperature in the volume of both sets of samples of course similar) has according the generally accepted Turnbull equation [43] (see Eq. 11) a positive influence on crystal growth:

$$u = f \cdot A \cdot \frac{T}{\eta} \cdot \left[1 - \exp\left(-\frac{B \cdot \Delta T}{T}\right) \right] \quad (11)$$

where u is the crystal growth rate, A and B are constants, T is temperature, ΔT is undercooling, η is viscosity and f is a model-based factor associated with the number of active sites on the crystal growth interface. Consequently, the growth-accelerating effect of the robust surface crystalline layer can be probably associated with the better cohesivity of nuclei with critical magnitude or lack of non-stationary flow conditions that would disrupt the diffusion of antimony towards the glass/crystal interface. If we would further assume the crystal growth in the $(\text{GeSe}_2)_{0.3}(\text{Sb}_2\text{Se}_3)_{0.7}$ glass proceeding similarly as in case of the $(\text{GeS}_2)_x(\text{Sb}_2\text{S}_3)_{1-x}$ glasses, i.e. in accordance with the 2-D nucleation-growth model [44], further evidence for the benefactory influence of the stationary flow conditions (provided by the robust crystalline layer surrounding the glass grain) would arise, since the 2-D nucleation-growth nucleation growth is particularly sensitive to the cluster lay-out on the crystal-glass interface and to the formation frequency (and stability) of the nuclei at this interface. [45]

Lastly, it should be stressed that the above analysis was derived for the initial non-equilibrium stages of the crystallization process, influencing position of the crystallization onset and the overall crystallization rapidity (as evidenced by the data in Figs. 1 and 2, and their kinetic quantification depicted in Fig. 4D). Taking into account the evolution of crystallization enthalpies depicted in Fig. 4A, it is clear that in the pseudo-equilibrium state, when the system was given enough time to achieve full crystallinity, the existence of the robust surface crystalline layer hinders the overall diffusion (having essentially the same effect as large number of mechanically induced defects – see the ΔH values for finest powders) and thus inhibits formation of fully crystalline material (in relation to the Sb_2S_3

content). Similar behavior was earlier observed for various chalcogenide materials during the thermomechanical (TMA) experiments, where the existence of robust surface crystalline layer together with the forced material flow inhibited crystal growth even in case of certain congruently crystallizing materials. [41, 46, 47]

6. Conclusions

Crystallization behavior of the $(\text{GeSe}_2)_{0.3}(\text{Sb}_2\text{Se}_3)_{0.7}$ glass was investigated in dependence on reaction atmosphere (pure N_2 versus air) and particle size. Presence of air was found to significantly accelerate the non-isothermal crystallization process and change its model-based kinetics – both the surface and volume crystal growths were affected. Based on the infrared microscopy observations and estimated viscosity of the material at crystallization temperature the following mechanism was proposed. Presence of oxygen activates the surface crystallization centers, which lead to formation of a relatively robust surface crystalline layer – the layer appears to further passivate the sample surface and prevents the macroscopic viscous flow. The quasi-stationary conditions then contribute to better cohesivity of critical nuclei and crystal/glass interface. However, long-term-wise the surface crystalline layer prevents the sample to reach full crystallinity (possibly by restricting the incongruent diffusion in the sample) as evidenced by the crystallization enthalpy reaching only ~ 75 % of the maximum value (obtained during the crystallization in N_2).

Acknowledgements

This work was supported by the Czech Science Foundation under project no. 17-11753S.

References

- [1] Q. Li, B. Mihailova, D. Creaser, J. Sterte, *Micropor. Mesopor. Mat.* 43 (2001) 51.
- [2] Z. Li, H. Hu, K.A. Khor, *J. Non-Cryst. Sol.* 445-446 (2016) 69.
- [3] D. Dudic, V. Djokovic, D. Kostoski, *Polym. Test.* 23 (2004) 621.

- [4] L. Zhang, S. Pauly, Z.W. Zhu, T. Gemming, H.M. Fu, J. Eckert, H.F. Zhang, *Intermetallics* 73 (2016) 5.
- [5] F. Steudel, A.C. Rimbach, S. Loos, B. Ahrens, S. Sweizer, *Radiat. Meas.* 90 (2016) 274.
- [6] T. Gheiratmand, H.R. Madaad-Hosseini, *J. Magn. Magn. Mater.* 408 (2016) 177.
- [7] P.K. Jha, O.P. Pandey, K. Singh, *J. Non-Cryst. Sol.* 440 (2016) 76.
- [8] J. Lu, Z. Lu, C. Peng, X. Li, H. Jiang, *Mater. Chem. Phys.* 148 (2014) 449.
- [9] R. Svoboda, J. Málek, *Thermochim. Acta* 579 (2014) 56.
- [10] D. Brandová, R. Svoboda, Z. Olmrová Zmrhalová, J. Chovanec, R. Bulánek, *J. Therm. Anal. Calorim.* – in press.
- [11] R. Svoboda, D. Brandová, *J. Therm. Anal. Calorim.* 129 (2017) 593.
- [12] R. Svoboda, *J. Non-Cryst. Sol.* 456 (2017) 88.
- [13] R. Svoboda, *J. Non-Cryst. Sol.* 452 (2016) 102.
- [14] P. Pustková, Z. Zmrhalová, J. Málek, *Thermochim. Acta* 466 (2007) 13.
- [15] J.H. Lee, J.H. Yi, W.H. Lee, B.J. Park, Y.G. Choi, *J. Non-Cryst. Sol.* 481 (2018) 21.
- [16] H. Parnell, D. Furniss, Z. Tang, N.C. Neate, T.M. Benson, A.B. Seddon, *J. Am. Ceram. Soc.* 101 (2018) 208.
- [17] H. Wang, G. Wang, D. Shi, X. Shen, Y. Lu, Q. Nie, *J. Non-Cryst. Sol.* 453 (2016) 108.
- [18] P. Němec, M. Olivier, E. Baudet, A. Kalendová, P. Benda, V. Nazabal, *Mater. Res. Bull.* 51 (2014) 176.
- [19] L. Tichý, H. Tichá, *Mat. Chem. Phys.* 152 (2015) 1.
- [20] E.R. Shaaban, I.B.I. Tomsah, *J. Therm. Anal. Calorim.* 105 (2011) 191.
- [21] R. Svoboda, D. Brandová, *J. Therm. Anal. Calorim.* 127 (2017) 799.
- [22] J. Šesták, *Thermophysical Properties of Solids, Their Measurements and Theoretical Analysis*, Elsevier, Amsterdam, 1984.
- [23] L. Petit, N. Carlie, K. Richardson, Y. Guo, A. Schulte, B. Campbell, B. Ferreira, S. Martin, *J. Phys. Chem. Sol.* 66 (2005) 1788.
- [24] V. Nazabal, P. Nemeč, A. M. Jurdyc, S. Zhang, F. Charpentier, H. Lhermite, J. Charrier, J. P. Guin, A. Moreac, M. Frumar, J. L. Adam, *Thin Solid Films* 518 (2010) 4941.
- [25] Z. G. Ivanova, E. Cernoskova, V. S. Vassilev, S. V. Boycheva, *Mater. Lett.* 57 (2003) 1025.
- [26] M. Wihl, M. Cardona, J. Tauc, *J. Non-Cryst. Sol.* 8-10 (1972) 172.
- [27] O. Matsuda, K. Inoue, K. Murase, *Sol. State Commun.* 75 (1990) 303.
- [28] K. Jackson, A. Briley, S. Grossman, D. V. Porezag, M. R. Pederson, *Phys. Rev. B* 60 (1999) 14985.
- [29] L. Petit, N. Carlie, R. Villeneuve, J. Massera, M. Couzi, A. Humeau, G. Boudebs, K. Richardson, *J. Non-Cryst. Sol.* 352 (2006) 5413.
- [30] J. Šesták, *Science of Heat and Thermophysical Studies: A Generalized Approach to Thermal Analysis*, Elsevier, Amsterdam, 2005.
- [31] S. Vyazovkin, A. K. Burnham, J. M. Criado, L. A. Pérez-Maqueda, C. Popescu, N. Sbirrazzuoli, *Thermochim. Acta* 520 (2011) 1.
- [32] J. Opfermann, *J. Therm. Anal. Calorim.* 60 (2000) 641.
- [33] M. Avrami, *J. Chem. Phys.* 7 (1939) 1103.
- [34] M. Avrami, *J. Chem. Phys.* 7 (1940) 212.
- [35] M. Avrami, *J. Chem. Phys.* 7 (1941) 177.
- [36] W.A. Johnson, K.F. Mehl, *Trans. Am. Inst. Min. (Metall) Eng.* 135 (1939) 416.
- [37] H. E. Kissinger, *Anal.Chem.* 29 (1957) 1702.

- [38] H. L. Friedman, Kinetics of Thermal Degradation of Char-Forming Plastics from Thermogravimetry. Application to a Phenolic Plastic, Wiley Subscription Services, Inc., A Wiley Company, New York, 1964.
- [39] J. Málek, Thermochemica Acta 355 (2000) 239.
- [40] R. Svoboda, J. Málek, Thermochemica Acta 526 (2011) 237.
- [41] Z. Zmrhalová, P. Pilný, R. Svoboda, J. Šhánělová, J. Málek, J. Alloys Compd. 655 (2016) 220.
- [42] P. Košťál, J. Málek, J. Non-Cryst. Sol. 353 (2007) 2803.
- [43] M.H. Cohen, D.J. Turnbull, J. Chem. Phys. 31 (1959) 1164.
- [44] G.L. Smith, M.C. Weinberg, Phys. Chem. Glasses 35 (1994) 6.
- [45] K.A. Jackson, D.R. Uhlmann, J.D. Hunt, J. Cryst. Growth 1 (1967) 1
- [46] J. Málek, Z. Zmrhalová, P. Honcová, J. Therm. Anal. Calorim. 105 (2011) 565.
- [47] R. Svoboda, D. Štrítecký, Z. Zmrhalová, D. Brandová, J. Málek, J. Non-Cryst. Sol. 445-446 (2016) 7.

Table 1

F-test values and correlation coefficients obtained from MKA simultaneous optimization of all DSC curves within the given dataset. F-crit = 1.03

nitrogen		F-test	r2
20	AC	1	0.99693
	NC	1.57	0.99453
	JMA	1.4	0.99525
125	AC	1.02	0.98936
	NC	1.07	0.9885
	JMA	1	0.98956
300	AC	1.02	0.982235
	NC	1.02	0.982339
	JMA	1	0.98271
bulk	AC	1.01	0.979319
	NC	1	0.979975
	JMA	1.02	0.979269

air		F-test	r2
20	AC	1	0.99677
	NC	1.36	0.995134
	JMA	1.02	0.996693
125	AC	1.02	0.988646
	NC	1	0.988561
	JMA	1.04	0.988241
300	AC	1.04	0.985735
	NC	1	0.987817
	JMA	1.02	0.986549
bulk	AC	1.01	0.964644
	NC	1	0.966267
	JMA	1	0.965469

Figure captions

Fig. 1: DSC crystallization peaks obtained for the 20 – 50 μm (left column) and 125 – 180 μm (right column) $(\text{GeSe}_2)_{0.3}(\text{Sb}_2\text{Se}_3)_{0.7}$ glassy powder fractions. Upper and

lower rows correspond to the measurements performed in air and in pure nitrogen, respectively. Exothermic effects evolve in the upwards direction.

Fig. 2: DSC crystallization peaks obtained for the 300 – 500 μm powder fraction (left column) and bulk samples of $(\text{GeSe}_2)_{0.3}(\text{Sb}_2\text{Se}_3)_{0.7}$ glass. Upper and lower rows correspond to the measurements performed in air and in pure nitrogen, respectively. Exothermic effects evolve in the upwards direction.

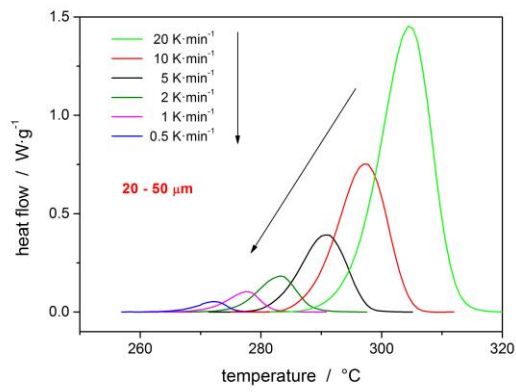
Fig. 3: A) Raman spectra for the as-prepared $(\text{GeSe}_2)_{0.3}(\text{Sb}_2\text{Se}_3)_{0.7}$ glass and powdered samples crystallized in DSC under different atmospheres.
B) XRD patterns of the DSC-crystallized $(\text{GeSe}_2)_{0.3}(\text{Sb}_2\text{Se}_3)_{0.7}$ powders under the two different atmospheres.

Fig. 4: A) The overall crystallization enthalpy ΔH evaluated in dependence on averaged particle size and type of reaction atmosphere for the studied $(\text{GeSe}_2)_{0.3}(\text{Sb}_2\text{Se}_3)_{0.7}$ powders and bulk ($d_{aver} = 1$).
B) The apparent activation energy E evaluated in dependence on averaged particle size and type of reaction atmosphere for the studied $(\text{GeSe}_2)_{0.3}(\text{Sb}_2\text{Se}_3)_{0.7}$ powders and bulk ($d_{aver} = 1$). Results provided by the original Kissinger and isoconversional Friedman methods are displayed.
C) Averaged kinetic parameters of the AC model evaluated in dependence on averaged particle size and type of reaction atmosphere for the studied $(\text{GeSe}_2)_{0.3}(\text{Sb}_2\text{Se}_3)_{0.7}$ powders and bulk ($d_{aver} = 1$).
D) Averaged maxima of characteristic kinetic functions $z(\alpha)$ and $y(\alpha)$ evaluated in dependence on averaged particle size and type of reaction atmosphere for the studied $(\text{GeSe}_2)_{0.3}(\text{Sb}_2\text{Se}_3)_{0.7}$ powders and bulk ($d_{aver} = 1$). Red dashed line indicates the theoretical “fingerprint” $\alpha_{max,z} = 0.632$ value characteristic for the JMA model.

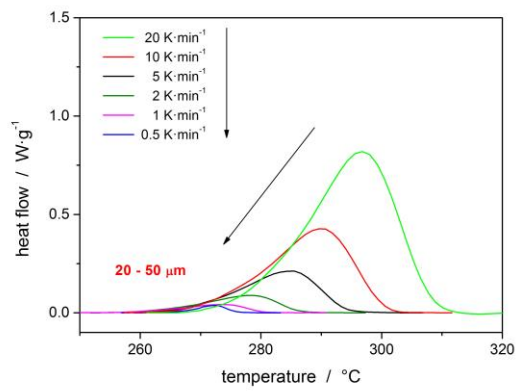
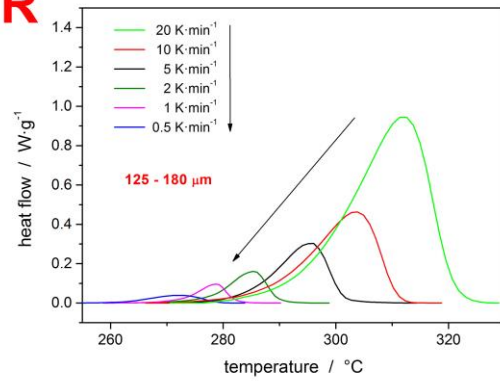
Fig. 5: A) Infrared micrograph of the bulk sample partially crystallized (heated up to 288 $^{\circ}\text{C}$) in N_2 – a surface view. The scale bar is 20 μm .
B) Infrared micrograph of the bulk sample partially crystallized (heated up to 288 $^{\circ}\text{C}$) in N_2 – a cross-section view. The scale bar is 100 μm .
C) Infrared micrograph of the bulk sample partially crystallized (heated up to 294 $^{\circ}\text{C}$) in N_2 – a surface view. The scale bar is 20 μm .
D) Infrared micrograph of the bulk sample partially crystallized (heated up to 294 $^{\circ}\text{C}$) in N_2 – a cross-section view. The scale bar is 50 μm .

Fig. 6: A) Infrared micrograph of the bulk sample partially crystallized (heated up to 288 $^{\circ}\text{C}$) in air – a surface view. The scale bar is 20 μm .
B) Infrared micrograph of the bulk sample partially crystallized (heated up to 288 $^{\circ}\text{C}$) in air – a cross-section view. The scale bar is 50 μm .
C) Infrared micrograph of the bulk sample partially crystallized (heated up to 294 $^{\circ}\text{C}$) in air – a surface view. The scale bar is 20 μm .
D) Infrared micrograph of the bulk sample partially crystallized (heated up to 294 $^{\circ}\text{C}$) in air – a cross-section view. The scale bar is 100 μm .

Fig 1



AIR



N_2

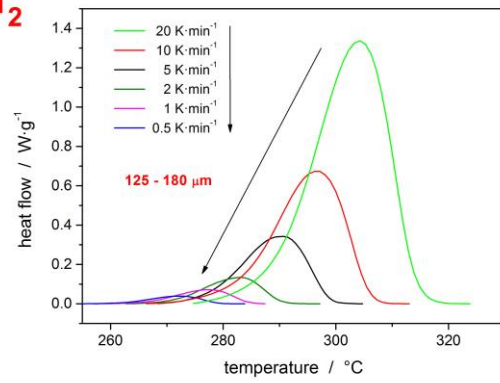
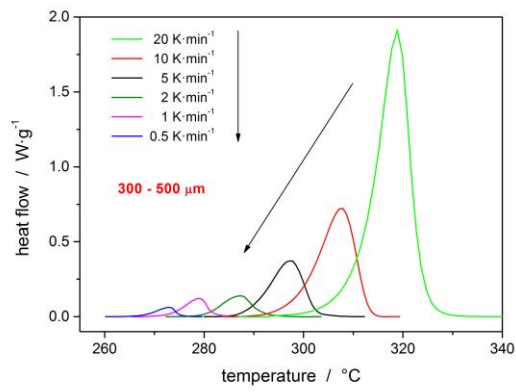
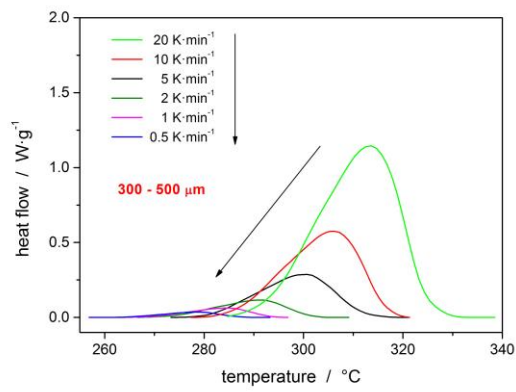
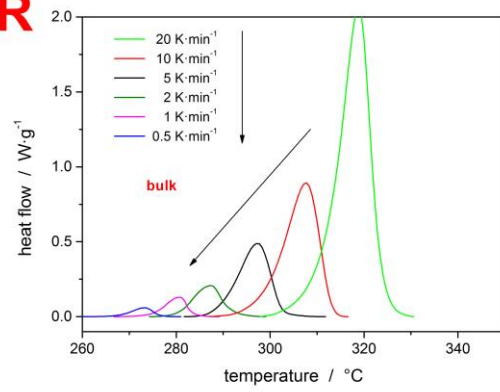


Fig 2



AIR



N_2

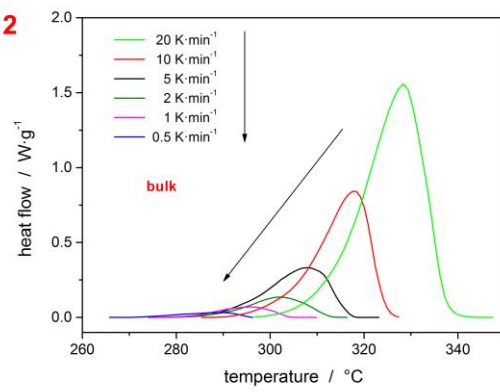


Fig 3

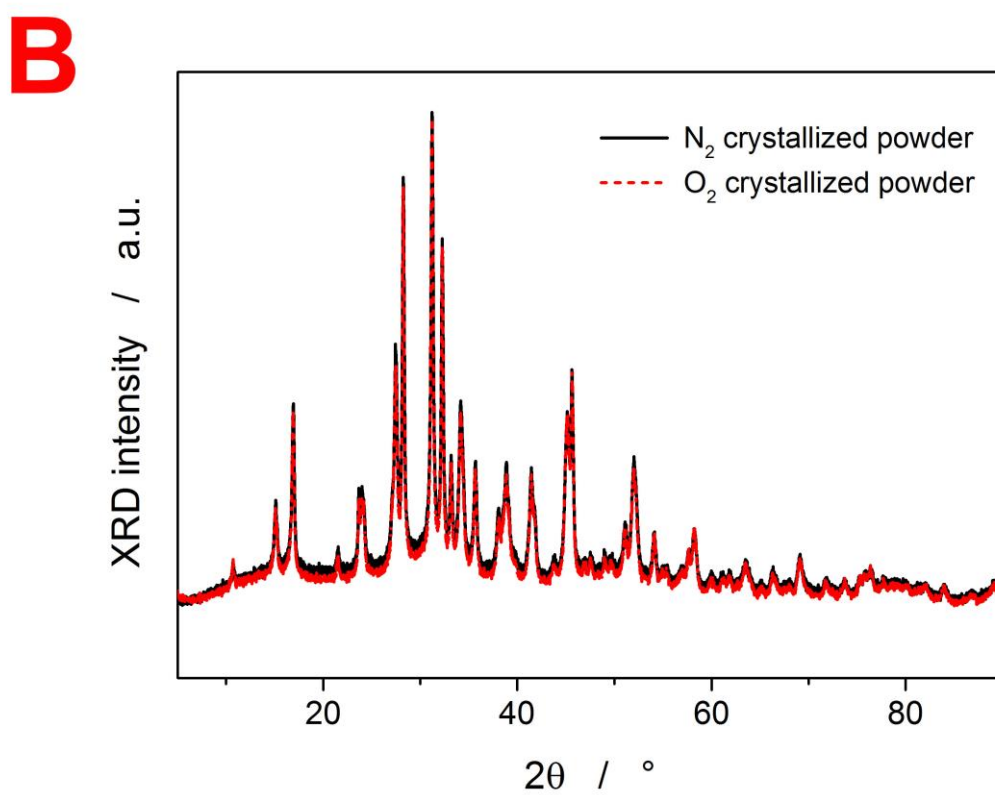
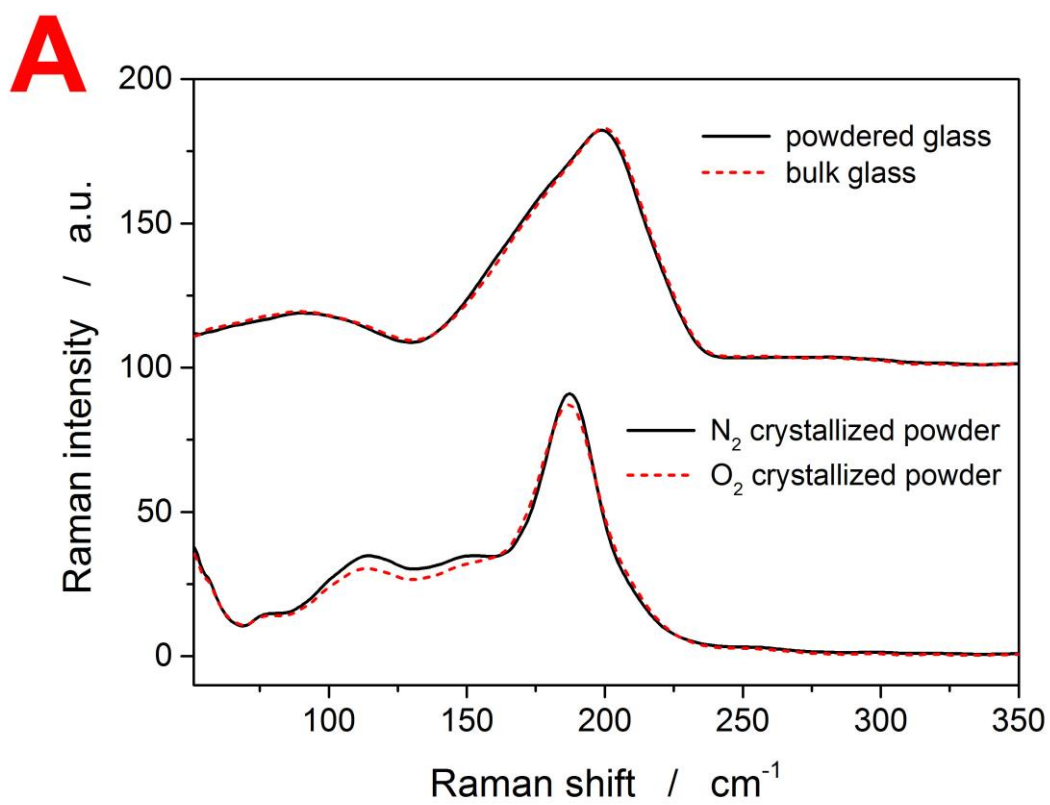


Fig 4

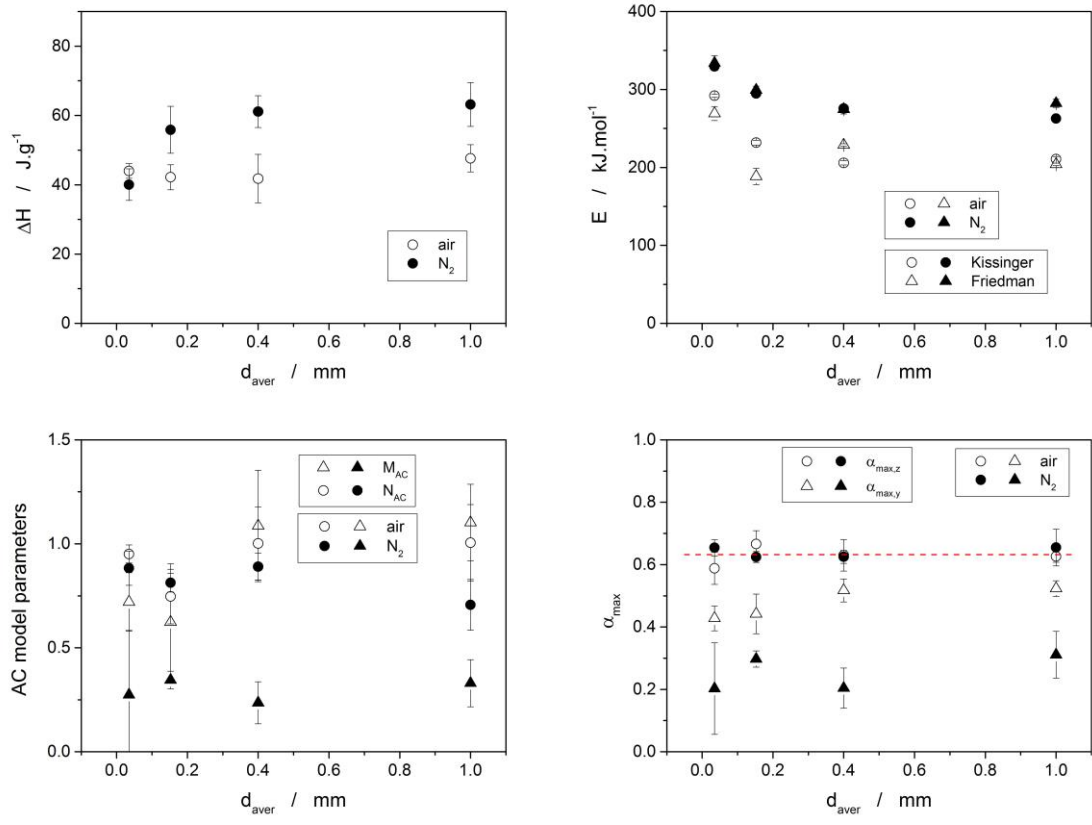


Fig 5

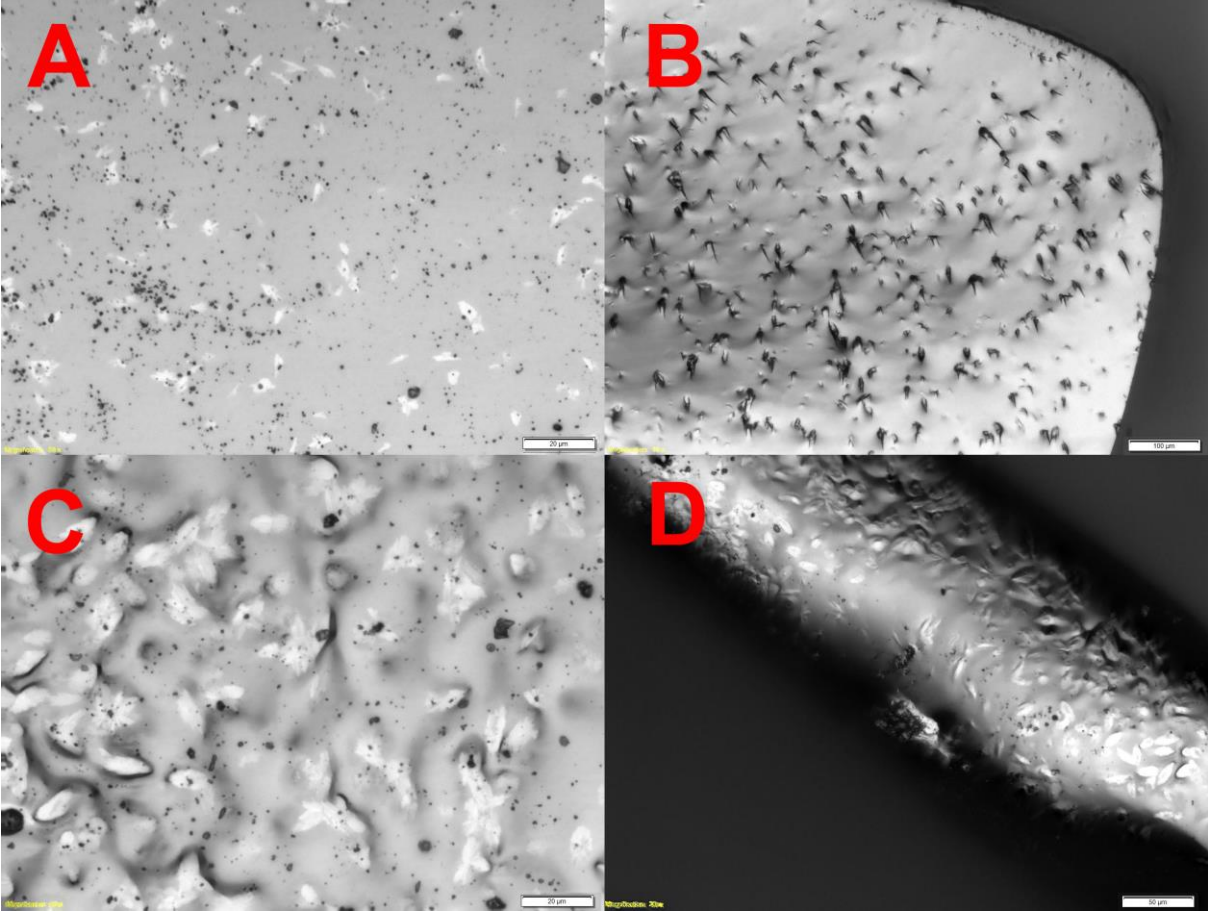


Fig 6

